UC Irvine
UC Irvine Previously Published Works

Title
Spatial profiling of the interplay between cell type- and vision-dependent transcriptomic programs in the visual cortex

Permalink
https://escholarship.org/uc/item/6vq1b3ps

Journal
Proceedings of the National Academy of Sciences of the United States of America, 122(7)

ISSN
0027-8424

Authors
Xie, Fangming
Jain, Saumya
Xu, Runzhe
et al.

Publication Date
2025-02-18

DOI
10.1073/pnas.2421022122

Copyright Information
This work is made available under the terms of a Creative Commons Attribution-NonCommercial-NoDerivatives License, available at https://creativecommons.org/licenses/by-nc-nd/4.0/

Peer reviewed

eScholarship.org Powered by the California Digital Library
University of California

PNAS RESEARCH ARTICLE | NEUROSCIENCE OPEN ACCESS

Spatial profiling of the interplay between cell type- and vision-dependent transcriptomic programs in the visual cortex

Fangming Xie[a,1,2], Saumya Jain[a,b,1], Runzhe Xu[a,1], Salwan Butrus[c,d], Zhiqun Tan[e], Xiangmin Xu[e], Karthik Shekhar[c,d,f,2], and S. Lawrence Zipursky[a,2]

Affiliations are included on p. 11.

Contributed by S. Lawrence Zipursky; received October 18, 2024; accepted January 7, 2025; reviewed by Uri Alon, Michael E. Greenberg, and Corey Harwell

How early sensory experience during "critical periods" of postnatal life affects the organization of the mammalian neocortex at the resolution of neuronal cell types is poorly understood. We previously reported that the functional and molecular profiles of layer 2/3 (L2/3) cell types in the primary visual cortex (V1) are vision-dependent [S. Cheng *et al.*, *Cell* 185, 311–327.e24 (2022)]. Here, we characterize the spatial organization of L2/3 cell types with and without visual experience. Spatial transcriptomic profiling based on 500 genes recapitulates the zonation of L2/3 cell types along the pial–ventricular axis in V1. By applying multitasking theory, we suggest that the spatial zonation of L2/3 cell types is linked to the continuous nature of their gene expression profiles, which can be represented as a 2D manifold bounded by three archetypal cell types. By comparing normally reared and dark reared L2/3 cells, we show that visual deprivation-induced transcriptomic changes comprise two independent gene programs. The first, induced specifically in the visual cortex, includes immediate-early genes and genes associated with metabolic processes. It manifests as a change in cell state that is orthogonal to cell-type-specific gene expression programs. By contrast, the second program impacts L2/3 cell-type identity, regulating a subset of cell-type-specific genes and shifting the distribution of cells within the L2/3 cell-type manifold. Through an integrated analysis of spatial transcriptomics with single-nucleus RNA-seq data, we describe how vision patterns cortical L2/3 cell types during the critical period.

cortex | transcriptomics | spatial transcriptomics | vision | gradients

Significance

Layer 2/3 (L2/3) glutamatergic neurons are important sites of experience-dependent plasticity and learning in the mammalian cortex. Their properties vary continuously with cortical depth and depend upon experience. Here, by applying spatial transcriptomics and different computational approaches in the mouse primary visual cortex, we show that vision regulates orthogonal gene expression programs underlying cell states and cell types. Visual deprivation not only induces an activity-dependent cell state, but also alters the composition of L2/3 cell types, which are appropriately described as a transcriptomic continuum. Our results provide insights into how experience shapes transcriptomes that may, in turn, sculpt brain wiring, function, and behavior.

Early sensory experiences influence the development of neural circuitry throughout the mammalian brain (1–3). In the primary visual cortex (V1), visual experience is required to establish the circuitry for binocular vision (4, 5). Vision-dependent development of binocular circuits occurs in mice after eye-opening [postnatal day (P) 14]. There are only a few binocular layer 2/3 (L2/3) neurons at eye opening and their number increases during the ensuing week. From P21 to P35, the tuning properties of these neurons improve markedly in a vision-dependent process. This developmental time window is referred to as the critical period (4, 6–8). Classically, the influence of early visual experience has not been examined at the level of the many cell types that form the building blocks of V1 circuitry. To address this gap, we previously performed single-nucleus RNA-seq (snRNA-seq) in normal- and dark-reared (NR, DR) mice during postnatal development, including the critical period (9–11). Using computational methods, we reconstructed the postnatal maturation of V1 cell types in NR mice and compared these profiles with DR mice. This enabled us to identify the cell types and gene expression programs impacted by vision. For most cell types, DR had little impact on molecular identity. However, DR had a pronounced effect on glutamatergic cell types in the supragranular layers (L) 2/3/4. In NR mice, L2/3 glutamatergic neurons comprise three molecularly distinct types (A, B, and C). These L2/3 types occupy three partially overlapping sublayers along the pial–ventricular axis of L2/3 (upper, middle, and lower, respectively) based on the in situ expression patterns of three marker genes. DR altered the expression patterns of these marker genes, and a comparison of transcriptome-based clusters in DR did not correspond to NR types. Based on these observations, we concluded that visual deprivation during the critical period selectively disrupted L2/3 cell types. Furthermore, visual deprivation regulated large groups of genes, including determinants of cell adhesion and synapse formation. However, as clusters in DR could not be matched to NR types, we could not separate vision-dependent changes in cell state

Author contributions: F.X., S.J., R.X., S.B., K.S., and S.L.Z. designed research; F.X., S.J., R.X., S.B., Z.T., X.X., and K.S. performed research; Z.T. and X.X. contributed new reagents/analytic tools; F.X., S.J., R.X., and S.B. analyzed data; S.L.Z. and K.S. supervising the research; and F.X., S.J., S.B., Z.T., K.S., and S.L.Z. wrote the paper.

Reviewers: U.A., Weizmann Institute of Science; M.E.G., Harvard Medical School; and C.H., University of California San Francisco.

The authors declare no competing interest.

Copyright © 2025 the Author(s). Published by PNAS. This open access article is distributed under Creative Commons Attribution-NonCommercial-NoDerivatives License 4.0 (CC BY-NC-ND).

[1]F.X., S.J., and R.X. contributed equally to this work.

[2]To whom correspondence may be addressed. Email: fmxie@ucla.edu, kshekhar@berkeley.edu, or lzipursky@mednet.ucla.edu.

This article contains supporting information online at https://www.pnas.org/lookup/suppl/doi:10.1073/pnas.2421022122/-/DCSupplemental.

Published February 13, 2025.

from vision-dependent changes in cell type, their organization, or both.

Here, we combined spatial transcriptomics and computational analyses to map the organization of L2/3 cell types in V1, and to assess the impact of visual deprivation on this organization. The gene expression changes due to visual deprivation comprise two independent transcriptomic programs. The first program is upregulated across multiple cell types throughout the visual areas and represents an activity-dependent cell state. The second program regulates a subset of cell-type-specific genes within L2/3, and its impact on cell type composition can be interpreted using multitasking theory (12), a recently proposed framework for analyzing gene expression continua. Thus, visual deprivation affects both activity-dependent transcriptomic states and cell-type composition in L2/3.

Results

Spatial Transcriptomic Analysis of V1 Reveals the Continuous Sublayered Arrangement of L2/3 Glutamatergic Cell Types. We first sought to explore the spatial arrangement of L2/3 cell types. To do this, we performed multiplexed error-robust fluorescence in situ hybridization [MERFISH (13)] on brain coronal sections containing V1 obtained from NR mice at P28 (Fig. 1*A*) (14). MERFISH is an imaging-based approach that allows simultaneous mapping of hundreds of genes in individual cells within an intact tissue section. Using computational methods, cells can be classified into types based on combinatorial gene expression patterns, and the spatial arrangement of each cell type can be visualized. For these experiments, we selected a panel of 500 genes that included cortical area- and layer-specific markers, marker genes for all major cortical cell populations (9, 15), and activity-regulated genes (16) (Datasets S1 and S2). Notably, given our specific goal of studying cell-type-specific changes within L2/3, we included 170 genes selected from the 286 L2/3 cell-type-identity genes we previously reported (9) (Dataset S1). These 170 genes includes all type-B-specific genes (n = 35/35), and more than half of the types A and C-specific genes (n = 135/251) selected with a preference on gene categories such as cell-surface molecules, synaptic factors, and transcription factors—factors that are related to neuronal cell type identity and function.

We performed a preliminary clustering of the cells from the entire section, defining clusters using a combination of molecular similarity and spatial proximity (*Materials and Methods*). This analysis identified 15 cell clusters, which highlighted different high-level anatomical structures of the mouse brain, including the neocortex with its characteristic laminar structure, parts of the hippocampus, and midbrain structures (*SI Appendix*, Fig. S1*A*). These associations were supported by in situ expression patterns of well-known genes. For example, *Slc17a7* (*Vglut1*), a marker for glutamatergic neurons, is prominently expressed in the cortex and parts of the hippocampus, two regions where glutamatergic neurons comprise 80 ~ 90% of all neurons (19–21) (*SI Appendix*,

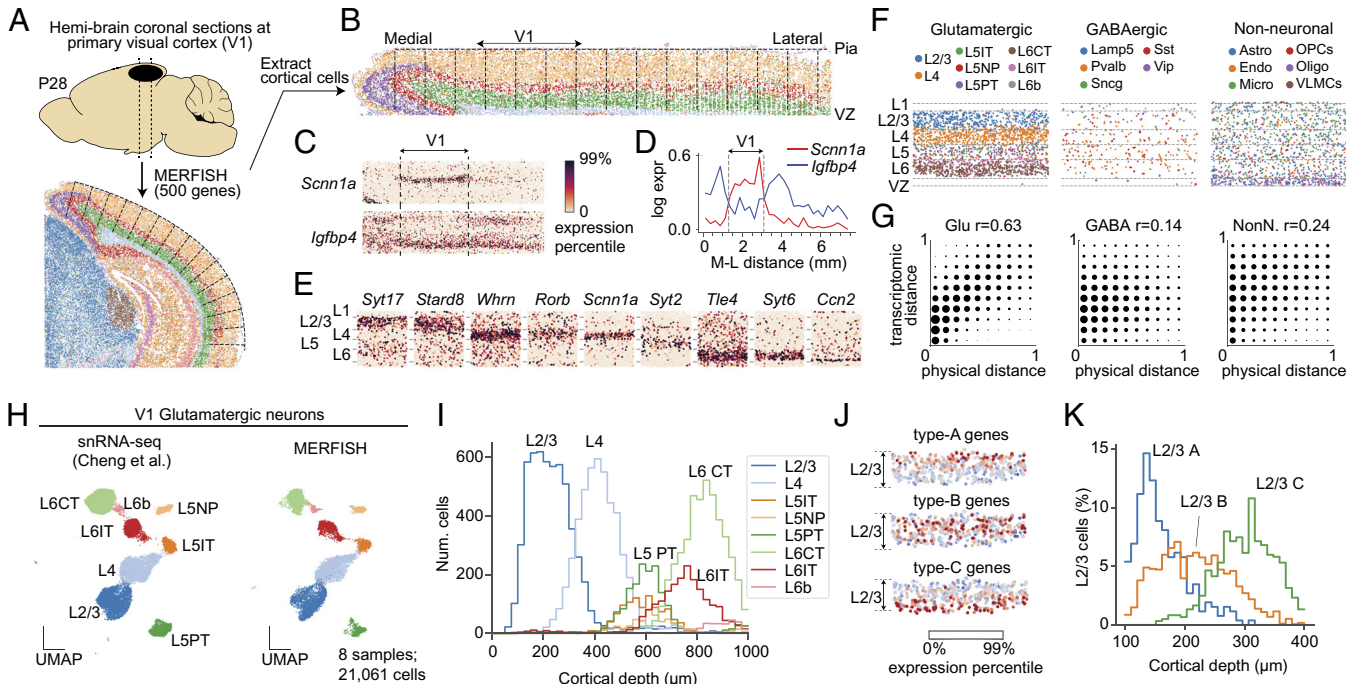

Fig. 1. MERFISH recapitulates the spatial organization of L2/3 glutamatergic neurons in V1. (*A*) MERFISH was performed on mouse coronal brain sections using a panel of 500 genes. The gene panel was designed to resolve cell types and cell states in V1 based on published studies (9, 15–17). The lower panel shows an overview of the MERFISH data, showing a thin (10 μm) coronal section including the neocortex, parts of the hippocampus, and midbrain structures. Individual cells are colored by their cluster membership based on both gene expression similarity and spatial proximity (see *SI Appendix*, Fig. S1*A* for a detailed annotation of these clusters). (*B*) Cortical cells with defined locations along the medial–lateral (M-L) and pial–ventricular (P-V) axis of the cortex. Tissue was straightened in silico to facilitate downstream analysis. Cells are colored as in panel *B*. (*C*) Two genes, *Scnn1a* and *Igfbp4* with area-specific in situ signatures. (*D*) Expression levels of genes in panel *E* along the M-L axis. The location of V1 is highlighted. (*E*) Examples of genes with layer-specific signatures in V1. (*F*) in situ organizations of subclasses of glutamatergic neurons (*Left*), GABAergic neurons (*Middle*), and nonneuronal cells (*Right*) in V1. (*G*) Correlations between physical distance and transcriptomic distance for pairs of glutamatergic (*Left*), GABAergic (*Middle*), and nonneuronal cells (*Right*) in V1. The sizes of the dots represent the density of cell pairs in decile bins. Physical distance is the difference in cell location along the cortical depth. Transcriptomic distance is the Euclidean distance in the space of top 10 principal components (PCs) derived from MERFISH genes. Both distances are normalized such that the minimum is 0 and maximum is 1. (*H*) Subclasses of V1 glutamatergic neurons are represented in UMAP embeddings obtained from integrating snRNA-seq (*Left*; ref. 9) and MERFISH (*Right*; this study) using Harmony (18). (*I*) Spatial distributions of glutamatergic subclasses along the cortical depth (P-V) axis. (*J*) Aggregated expression in V1 L2/3 for gene groups defining types A (n = 64 genes), B (n = 35 genes), and C (n = 71 genes). Type A, B, and C genes are distributed in *Upper*, *Middle*, and *Lower* L2/3, respectively. Colors represent gene expression levels going from 0 to 99 percentile. (*K*) Spatial distributions of types A, B, and C along the cortical depth spanning L2/3. MERFISH cell labels were transferred from previously published snRNA-seq data (9).

Fig. S1*B*). In contrast, *Gad1*, a marker for GABAergic neurons, is expressed at low levels in the cortex but high levels in the midbrain, where inhibitory neurons represent ~50% of neuronal cells (20, 21). *Sox10*, a marker for oligodendrocytes, is enriched in the white matter beneath the cortex.

We used the pial surface to define the tangential (medial–lateral) and vertical (pial–ventricular) coordinates of each cell and demarcated areas of the neocortex (Fig. 1 *B*–*G*). We localized the primary visual cortex (V1) based on the enrichment of *Scnn1a* and the depletion of *Igfbp4* along the tangential axis. Both markers, described previously (15, 17), allowed us to identify V1 as a ~2 mm wide × 1 mm deep region (Fig. 1 *C* and *D*). Within V1, we identified many genes expressed in a layer-specific fashion (Fig. 1*E*).

We used an integrative approach to classify each V1 cell in MERFISH into one of three classes (excitatory neurons, inhibitory neurons, and nonneuronal cells) and each neuron into one of 12 subclasses, as in ref. 9 (Fig. 1*F* and *SI Appendix*, Fig. S1 *C*–*E*). The relative frequencies of the subclasses tightly corresponded between MERFISH and snRNA-seq (Spearman correlation = 0.95) (Fig. 1*H* and *SI Appendix*, Fig. S1 *C*–*E*). The three cell classes in V1—glutamatergic neurons, GABAergic neurons, and nonneuronal cells—have distinct transcriptomic and spatial organizations. Different subclasses of glutamatergic neurons were spatially localized within expected layers along the pial–ventricular axis, where physical proximity implies transcriptomic similarity (Fig. 1 *F*–*I* and *SI Appendix*, Fig. S1*F*). By contrast, GABAergic neurons and nonneuronal cells are distributed more in a salt-and-pepper pattern with only weak correlations between physical and transcriptomic distance (Fig. 1 *F* and *G*).

Previously, we found that L2/3 cells can be clustered into three types (L2/3A, L2/3B, and L2/3C). Individual marker genes for these types—*Cdh13* for L2/3A, *Trpc6* for L2/3B, and *Chrm2* for L2/3C—were expressed in upper, middle, and lower regions of L2/3 along the pial–ventricular axis (9). However, the MERFISH data allowed us to validate the three-layered zonation of L2/3 types using a much larger gene panel (Fig. 1*J* and *SI Appendix*, Fig. S2). Combinatorial gene signatures based on 170 type-identity genes enabled classification of MERFISH L2/3 cells as L2/3A, L2/3B, or L2/3C. As expected, soma of the three cell types localized to the upper, middle, and lower sublayers within L2/3 (Fig. 1*K*). Type A and C identity genes were expressed in a more restricted spatial pattern, whereas type B identity genes were expressed more broadly.

Multitasking Theory Relates the Spatial Zonation of L2/3 Glutamatergic Neuronal Types to Their Continuous Transcriptomic Variation. Rather than forming three discrete transcriptomic cell types, L2/3 glutamatergic neurons form a continuum. This is most evident when we analyzed the data using diffusion pseudotime (DPT) (22), an approach based on diffusion maps (23). For snRNA-seq, DPT orders cells according to their type identity along the *x* axis and their corresponding type-identity genes along the *y* axis (Fig. 2*A*). The genes are expressed at different levels in a graded fashion, with no clear boundaries between the domains of each cell type. DPT produces a similar result for the MERFISH dataset, with cells now ordered based on their location along the cortical depth Fig. 2*B*), further supporting the link between continuous transcriptomic variation and spatial zonation.

Strikingly, such a link is predicted by a recently proposed framework known as multitasking theory (12, 24, 25). This theory posits that "if gene expression lies on a D-dimensional manifold (e.g., D = 3 for a tetrahedron, D = 2 for a triangle, or D = 1 for a line), the cells should show at least a D-dimensional spatial zonation [in tissue]" (12). Applying this framework to our data, we find that L2/3 neurons lie on a V-shaped manifold along the first two PCs, which is bounded by a triangle (Fig. 2*C* and *Materials and Methods*) (26). The structure of the manifold and the coordinates of the bounding triangle are similar for both the snRNA-seq and the MERFISH datasets (Fig. 2*D* and *SI Appendix*, Fig. S3). According to multitasking theory, vertices of the triangle represent "archetypal" cell types, with the gene expression profile of each archetype specialized for a particular function (see below). Indeed, the three vertices map to the L2/3 A, B, and C types identified by clustering, and cells inside the triangle are mixtures of the archetypal gene expression profiles (Fig. 2 *E* and *F*). Finally, consistent with the theory, the organization along the manifold from A to B to C is mirrored in the spatial zonation along the pial–ventricular axis (Fig. 1 *J* and *K*). This link between transcriptomic and spatial organization can also be shown by examining the distribution of the "physical distance" vs. "task distance" for pairs of L2/3 cells (25). We find a correlation between cortical depth and task distance along PC1, reflecting the spatial arrangement of types A-C along L2/3 sublayers (*SI Appendix*, Fig. S4*A*). By contrast, the correlation is weaker along PC2, suggesting type B has a more "salt-and-pepper" organization (*SI Appendix*, Fig. S4*B*).

We performed additional analyses to assess the robustness of the V-shaped manifold and the bounding triangle. Repeating the analyses with subsets of cells or genes resulted in only minor perturbations of the bounding triangle (Fig. 2 *G* and *H*). Repeating the analyses with shuffled versions of the original gene expression matrix further substantiated the continuous nature of the transcriptomic variation. First, we shuffled gene expression values independently for each gene across L2/3 cells, which preserves individual gene expression distributions while disrupting their correlations. This resulted in all cells collapsing toward the center and a total disruption of the triangular structure ($P < 0.001$; t-ratio test) (Fig. 2*I* and *SI Appendix*, Fig. S5). We then shuffled gene expression values independently for each gene within each cell type (Fig. 2*J*). This procedure distinguishes between two scenarios: a genuine continuum vs. discrete types seemingly continuous due to noise in the data, which could arise from the intrinsic stochasticity of gene expression or sampling noise in single-cell sequencing (27). When applied to clusters that span a continuum, the shuffling procedure splits continua into discrete clusters as long as the level of noise in the data is low to intermediate (*SI Appendix*, Fig. S6 *A*, *C*, and *E*). In contrast, when the clusters are already discrete it has no effect regardless of noise level (*SI Appendix*, Fig. S6 *B*, *D*, and *F*). Applying this shuffling procedure to our data splits L2/3 cells into three clusters (Fig. 2*J*), supporting that transcriptomic continuum is genuine and not an artifact of noise.

In addition to statistical robustness, we find several transcription factors (TFs), such as *Meis2*, *Rfx3,* and *Foxp1,* to be differentially expressed across archetypes consistently during different developmental times (*SI Appendix*, Fig. S7 *A* and *B*). The patterns of these TFs resemble "terminal selector transcription factors" which define neuronal cell type identity (28). These observations suggest that the transcriptomic diversity among L2/3 cells represent genuine cell types rather than transcriptional noise or transient cell states.

What is the functional significance of this continuum? According to multitasking theory, such transcriptomic continua arise as an optimal solution for division of labor among cells in tissues where a cell's functional identity is related to its spatial position. While the theory does not specify these functions, examining the genes that define the archetypes may provide some clues. By performing gene ontology (GO) analyses, we found that archetype-defining genes are enriched for biological processes related to neuronal development and functions (*SI Appendix*, Fig. S7*C*). Programs involved in neural wiring,

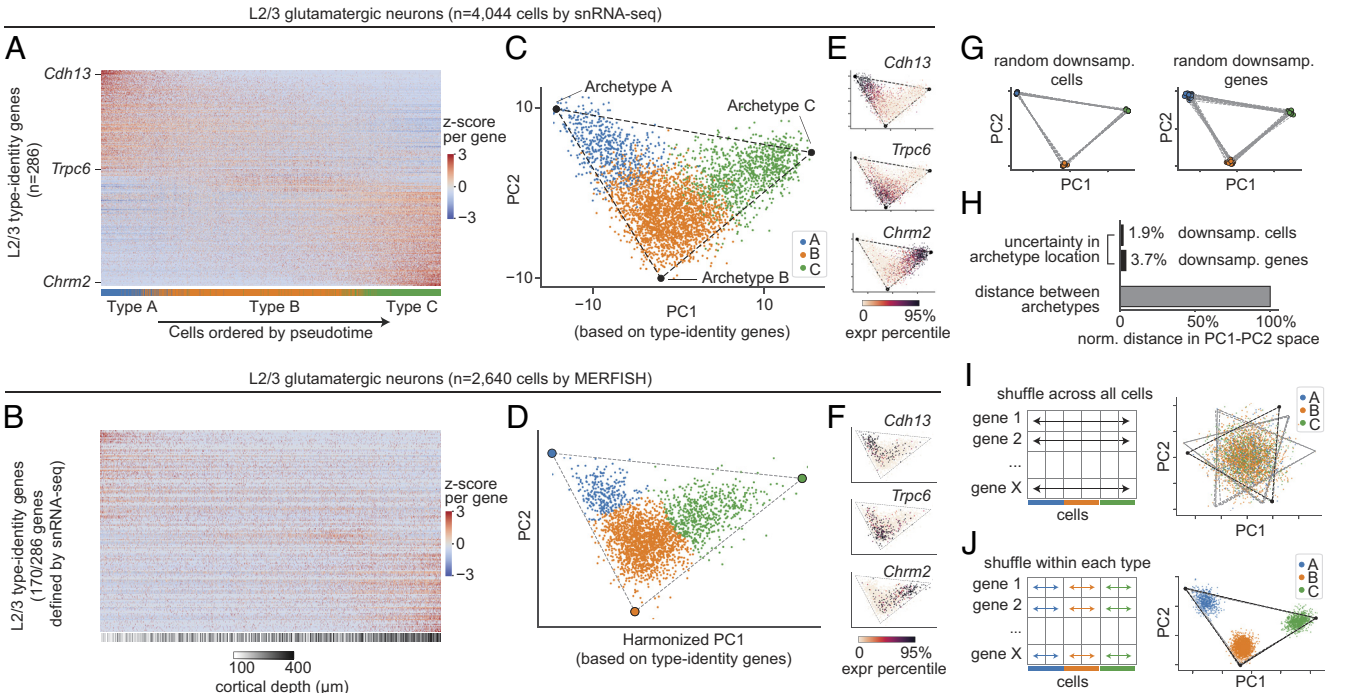

Fig. 2. L2/3 glutamatergic neurons form a continuous manifold bounded by a triangle, whose vertices represent archetypes. (*A* and *B*) Expression heatmaps of type-identity genes (Dataset S1) across L2/3 glutamatergic neurons for snRNA-seq (*A*) and MERFISH (*B*). Expression was quantified as z-scored, log-, and size-normalized counts. Z-scores were applied for each row (gene) across columns (cells). Cells (*x* axis) were ranked by diffusion pseudotime and colored by cell-type identity in (*A*) and cortical depth in (*B*) (annotation bar, *Bottom*). (*C* and *D*) L2/3 cells represented in PC1 and PC2 space based on the same type-identity genes in *A* and *B*. Cells are colored by type. The bounding triangle was inferred using computational procedures described by Adler et al. (12) (*Materials and Methods*). (*E* and *F*) Expression levels of *Cdh13*, *Trpc6,* and *Chrm2* in PC1/PC2 space for scRNA-seq (*E*) and MERFISH (*F*). (*G* and *H*) Stability of the bounding triangle over randomized trials involving random down-sampling of the original dataset to 80% of cells (*G*, *Left*) or 80% of genes (*G*, *Right*). Comparison % variation in archetype coordinates during randomizations relative to the typical interarchetype distances in these trials. Distances are measured by Euclidean distance in PC1-PC2 space (*H*). (*I* and *J*) L2/3 cells in PC1/PC2 space after shuffling each gene independently across all cells (*I*), and after shuffling each gene independently across cells within each type (*J*), respectively. The gray lines represent triangular fits using 80% of cells, randomly down-sampled ten times independently. Thus, these cells form a continuum of types rather than three noisy cell types (*SI Appendix*, Fig. S5). Panels *G*–*J* used snRNA-seq data only.

including "axon guidance" and "cell–cell adhesion," show up in all three types (A, B, and C). For example, among known cell-recognition molecules related to neural wiring, type A expresses *Cdh13, Cntn5, Epha6, Sema6a,* and *Robo1*; type B expresses *Epha3* and *Sema4a;* and type C expresses *Cdh12, Cntn2,* and *Robo3* (Dataset S3). The differential expression of these genes may be related to the distinct projection patterns of A, B, and C types to the higher visual areas (9, 29). Other programs, such as "sensory perception of light stimulus" and "detection of mechanical stimulus involved in sensory perception," are specific to types B and C, respectively. Although one can only speculate on the functional meaning at this stage (*Discussion*), the manifold representation of L2/3 neurons proves useful in understanding global and cell-type-specific changes due to visual deprivation, which we analyze in the next section.

Transcriptomic Heterogeneity in Vision-Deprived L2/3 Neurons Involves Two Distinct Gene Programs. To characterize the changes induced by visual deprivation, we obtained MERFISH data from mice DR between P21 to P28, following our published experimental protocol (Fig. 3*A* and *Materials and Methods*) (9). Comparisons of DR and NR sections collected at P28 showed an upregulation of 13 genes (FC > 2, FDR < 0.05, *SI Appendix*, Fig. S8*A*), a small subset of vision-dependent genes detected by snRNA-seq (see below). All 13 genes were canonical immediate early genes (IEGs) (16), and their upregulation was localized to the visual areas (Fig. 3*B*). Along the tangential axis, IEG levels were significantly higher in V1 than in its flanking regions (Fig. 3 *C* and *D* and *SI Appendix*, Fig. S8*B*). Consistent with prior snRNA-seq data, we observed that the upregulation of IEGs was broadly shared by most neuronal subclasses, albeit the induction is subtler in inhibitory neurons than excitatory neurons (*SI Appendix*, Fig. S8 *D* and *E*). Spatially, the upregulation of IEGs is visible throughout the cortical depth (Fig. 3 *C* and *E* and *SI Appendix*, Fig. S8*C*). Within L2/3, canonical IEGs, such as *Fos*, *Nr4a2, Junb, and Egr4*, were up-regulated in DR similarly in all sublayers (Fig. 3*F* and *SI Appendix*, Fig. S9 *A* and *C*).

We previously reported that DR selectively disrupts the transcriptomic signatures of L2/3 cell types in single-nucleus (sn) RNA-seq data from V1 (9). Our results were based on unsupervised clustering of snRNA-seq profiles from NR and DR mice. Most cell types correspond 1:1 between NR and DR with the notable exception of L2/3 neurons. In the MERFISH data, while type-identity genes by and large maintained their sublayered expression, they also exhibited some vision-dependent alterations in DR. L2/3A-specific genes were relatively unchanged, but L2/3B- and L2/3C-specific genes were downregulated (Fig. 3*G* and *SI Appendix*, Fig. S9 *B*–*D*). Taken together, Fig. 3 *A*–*G* suggest that vision impacts L2/3 transcriptomes in two distinct modes, one comprising broadly expressed genes (e.g. IEGs), and the other impacting genes associated with cell type identity (*SI Appendix*, Fig. S9 *E* and *F*).

These results motivated a reanalysis of our published snRNA-seq dataset (9). We combined NR and DR datasets at P28 and applied principal component analysis (PCA) using 6,360 highly variable genes (*Materials and Methods*). We focused on the top four PCs, which exhibited a clear spectral gap from other components (*SI Appendix*, Fig. S10*A*). PC1 and PC2 separated cells by rearing condition (NR vs. DR mice), while NR and DR cells intermixed in the PC3 to PC4 space (Fig. 3*H* and *SI Appendix*, Fig. S10 *B* and *C*).

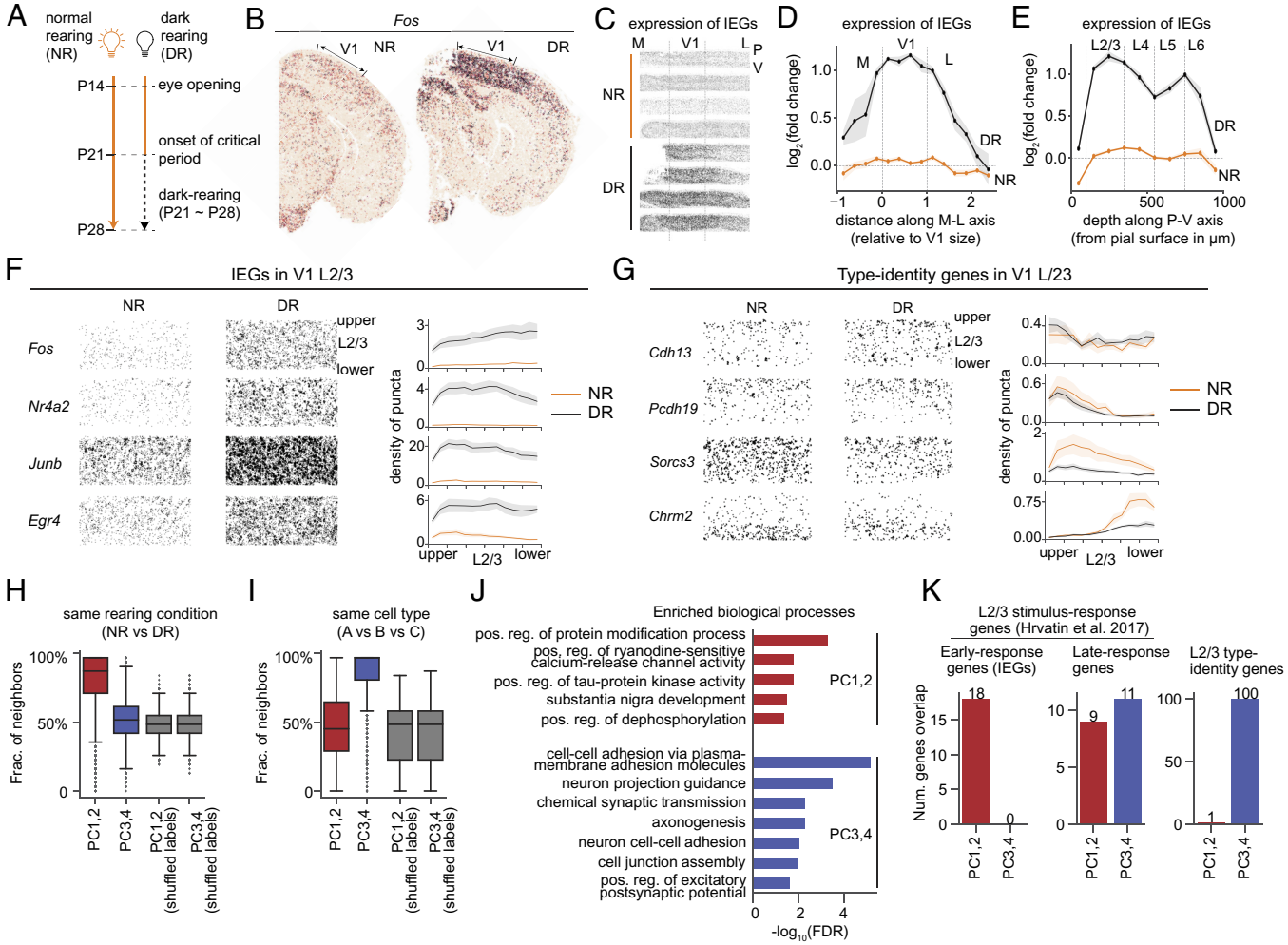

Fig. 3. Gene programs driving transcriptomic heterogeneity in normal- and dark-reared L2/3 neurons. (*A*) Protocol for dark-rearing (9). (*B*) In situ expression patterns of *Fos* in NR and DR coronal sections. Locations of V1 are highlighted. (*C*) Aggregated in situ expression of IEGs (16) in NR and DR in V1 and its flanking cortical regions. Rows in each condition correspond to biological replicates. (*D* and *E*) Aggregated expression of IEGs along the M-L axis (*D*) and the P-V axis (*E*). Fold change is quantified relative to the mean expression level over the entire V1 region for all NR samples. (*F* and *G*) In situ expression of representative IEGs (*F*) and type-identity genes (*G*). Individual dots are transcript molecules detected by MERFISH. Line plots show the distribution of puncta along the P-V axis from upper to lower L2/3. The density of puncta was defined as the number of puncta per 100 μm^2 area averaged across samples. Error bars represent SEM. (*H* and *I*) Distribution of L2/3 cells' neighbor identities in terms of the fraction of k nearest neighbors (k = 30) that are of the same rearing condition (NR vs. DR; panel *H*) and of the same type (A vs. B vs. C; panel *I*). PCs are computed from n = 6,360 HVGs (*Materials and Methods* and *SI Appendix*, Fig. S10). (*J*) GO analysis shows biological processes enriched in genes driving PC1 to PC2 (in red) and PC3 to PC4 (in blue). Raw results from the enrichment analysis were filtered to remove redundant terms (*Materials and Methods*). A full list of the top 10 significant GO terms with FDR < 0.05 is shown in *SI Appendix*, Fig. S10*E*. Top 100 genes for each PC ranked by the absolute value of PC loadings are used. (*K*) Overlap between PC-driving genes and previously defined gene groups. Activity-regulated genes, including early response genes (IEGs) and late-response genes in L2/3 glutamatergic neurons are from ref. 16. Type-identity genes from ref. 9 are listed in Dataset S1.

Conversely, PC3 to PC4, but not PC1 to PC2, separated NR cells by type identity (Fig. 3*I* and *SI Appendix*, Fig. S10 *B* and *C*), recapitulating the triangular manifold in Fig. 2*B*, which was estimated using 286 type-identity genes. Thus, transcriptomic variation in L2/3 glutamatergic neurons is driven by two gene programs: The first, encoded in PC1 to PC2, captures vision-dependent changes, while the second, encoded in PC3 to PC4, captures cell type identity.

As PCs are derived from orthogonal directions in transcriptomic space, we hypothesized that the gene programs encoded in PC1 to PC2 vs. PC3 to PC4 represent distinct biological processes. GO analysis shows that genes driving PC1 and PC2 were enriched in the regulation of protein modification and signaling pathways (Fig. 3*J* and *SI Appendix*, Fig. S10*E*), likely reflecting shifts in cell state due to experience-dependent activity. By contrast, PC3 and PC4 were enriched for genes associated with cell–cell adhesion, axonogenesis, neuron projection guidance, and chemical synaptic transmission (Fig. 3*J*, *SI Appendix*, Fig. S10*E*, and Dataset S4), which are associated with neuronal cell-type identity (30–33). We also compared the top-loading genes within each PC with a list of known activity-regulated genes in L2/3 glutamatergic neurons from Hrvatin et al. (16). This list includes 42 "early-response" genes, among which many are canonical IEGs, that were conserved across cell types in the original study, and 37 "late-response" genes, which were largely cell-type-specific (Dataset S5). PC1 to PC2 genes strongly overlapped with IEGs (odds ratio = 25, $P < 10^{-10}$; Fisher's exact test; significant enrichment) and barely overlapped with type-identity genes (odds ratio = 0.1, $P = 0.002$; Fisher's exact test; significant depletion) (Fig. 3*K* and *SI Appendix*, Fig. S10*F*). By contrast, PC3 to PC4 genes did not contain IEGs and significantly overlapped with type-identity genes (odds ratio = 40, $P < 10^{-10}$). Late-response genes featured in equal numbers across PC1 to PC2 and PC3 to PC4.

These results highlight the consistency between the MERFISH and the snRNA-seq datasets and present the following overall picture. The transcriptomic variance in NR and DR layer 2/3 cells can be decomposed into two independent programs: 1) PC1 to PC2, associated with experience-regulated cell states, and 2) PC3

to PC4, associated with cell type identity. However, we find that the contribution of these programs to the overall variance within a dataset differs by rearing condition. For NR, the projected variance along PC3 to PC4 is 2.9-fold higher than that along PC1 to PC2. By contrast, for DR, the projected variance along PC1 to PC2 is 2.8-fold higher than along PC3 to PC4. This disparity, however, drives the lack of correspondence in the highly- variable-gene-based clustering of NR and DR L2/3 neurons reported by Cheng et al. (9). Consistent with this, a "focused" clustering of DR L2/3 neurons using the 286 type-identity genes recovers cell clusters corresponding 1:1 with types A, B, and C in NR (*SI Appendix*, Fig. S11). Overall, this suggests that despite being masked by experience-dependent changes, cell identity programs persist in DR (*SI Appendix*, Fig. S10*D*), albeit with major alterations (Fig. 3*G*). We now analyze these alterations.

Visual Deprivation Alters the Composition of L2/3 Cell Types along the Transcriptomic Continuum. We used the 2D manifold representation (Fig. 2 *C* and *D*) to study cell-type-specific changes induced by visual deprivation. We hypothesized that vision could regulate one or more of the following features: a) the locations of the archetypes, i.e., the bounding triangle; b) the distribution of cells along the manifold, which correspond to changes in cell type composition and spatial zonation; and c) the expression levels of one or more type-identity genes.

To evaluate whether archetype coordinates change, we recalculated PCs based on the 286 type-identity genes as in Fig. 2*C*, but now using both NR and DR cells from the published snRNA-seq data. Using this representation, we separately inferred archetype coordinates using cells from each biological sample (n = 4 replicates for each condition, including P38 data from ref. 9). These calculations verified that L2/3 cells from NR and DR mice occupy similar triangular regions, with no significant changes detected in archetype coordinates (3 ~ 10% changes relative to the minimum distance between archetypes) (*SI Appendix*, Fig. S12 *A* and *C*).

Individual cells, however, distributed differently between NR and DR, shifting away from the region proximal to archetype B toward archetype A, and away from archetype C in DR (Fig. 4*A* and *SI Appendix*, Fig. S12*B*). This reorganization between NR and DR was also predicted by two alternative methods: optimal transport analysis (34, 35) (Fig. 4*B* and *Materials and Methods*) and supervised classification-based label transfer from NR to DR cells (Fig. 4*C*). The compositional difference between NR and DR at P28 or P38 was larger than the difference between P28NR and P38NR, or between P28DR and P38DR (*SI Appendix*, Fig. S12*D*). This suggests that the effect of DR on L2/3 transcriptomic identities is consistent over at least ten days. Furthermore, similar changes in cell type composition were also recovered in the MERFISH data (*SI Appendix*, Fig. S13). Additionally, MERFISH shows that the overall expression levels of type B and C genes decrease in DR, especially in middle and lower L2/3 (Fig. 4 *D* and *E* and *SI Appendix*, Fig. S14). By contrast, the expression of type A genes is relatively unchanged and consistently enriched in upper L2/3.

We performed differential gene expression analysis between NR and DR samples to identify vision-dependent genes within each type. In total, we identified 386 unique vision-dependent genes, of which 70 were regulated in type A, 226 in type B, and 304 in type C (fold change > 2 and FDR < 0.05). These genes included 90% (n = 38/42) of previously identified L2/3 IEGs (16), while the IEGs represent ~10% (n = 38/386) of the vision-dependent genes (Fig. 4*F* and Dataset S6). Moreover, most vision-dependent genes (90%; n = 348/386) are not type-specific, and they were up- or down-regulated in all or two of the three L2/3 types in DR (Fig. 4 *F–H*). Conversely, most type-identity genes (87%; n = 248/286) were vision-independent, consistently marking types A, B, and C in NR and DR (Fig. 4 *F* and *G*). Of 286 type-specific genes, 38 (13%) were vision-dependent (Fig. 4 *F* and *I*). These *vision-dependent type-identity* genes fell into six groups based on their patterns of regulation (Fig. 4*I*). Overall, type A had smaller fold changes in DR compared with types B and C in almost all genes. Unlike types B and C-specific genes, a group of type A genes (Group 2; n = 9) were up-regulated in types B and C, but did not change in type A themselves. The changes in individual type-identity genes were consistent with the overall trend that type A was less affected by DR than types B and C.

Together, these results exemplify the plasticity of the transcriptional programs defining A, B, and C cell types, resulting in a redistribution of cells in the 2D manifold associated with type identity due to visual deprivation (Fig. 4*J*). The nature of this redistribution is consistent across biological replicates of snRNA-seq (*SI Appendix*, Fig. S12) and MERFISH (*SI Appendix*, Fig. S13). Finally, L2/3 glutamatergic neurons (also known as L2/3 intratelencephalic neurons; L2/3 IT) are more sensitive to vision than deeper-layer intratelencephalic (L5/6 IT) neurons, consistent with prior results (9) (*SI Appendix*, Fig. S15).

Discussion

We previously showed that vision deprivation selectively impacts L2/3 glutamatergic neuronal types in V1 (9). Using unsupervised clustering of snRNA-seq data, we found that L2/3 neuronal clusters in DR mice "poorly resembled the three types in NR animals, and the expression patterns of cell-type-specific marker genes were disrupted". We interpreted these results as "*a global disruption of gene expression patterns throughout L2/3*", resulting in "*the loss of [L2/3] cell type identity in animals deprived of light*". The nature of the disruption in gene expression was, however, not clear due to our inability to relate cell types between the two conditions. In this study, we set out to resolve this issue.

Here, combining spatial transcriptomics with additional computational analyses enabled us to relate L2/3 cell types between NR and DR and thereby clarify the vision-dependent gene expression changes. We showed that visual deprivation impacts two orthogonal gene programs, one associated with experience-induced cell states and the other overlapping with programs of cell type identity. The deprivation-induced state changes dominate the transcriptomic variation in DR, masking cell type distinctions in the unsupervised clustering analysis used previously.

Using multitasking theory, we showed that the transcriptomic variation among L2/3 cells can be represented as a continuous manifold in 2D bounded by a triangle whose vertices represent archetypes A, B, and C. These archetypes represent the "basis sets" used to construct the profiles of sampled L2/3 neurons. While preserving the archetypes themselves, dark-rearing redistributes cells within the manifold, shifting cells away from archetypes B and C. Thus, L2/3 cell types are not lost in animals deprived of light, but their composition is altered, and the underlying gene expression programs are masked by orthogonal activity-induced changes. These changes are consistently reproduced in both MERFISH and snRNA-seq datasets.

A key tenet of multitasking theory is to link transcriptomic continua to the spatial zonation of functionally distinct cell types. Previous observations indicate that neurons within different L2/3 sublayers (A, B, C) differ in their functional properties and projections to higher visual areas (9, 16, 36). Our results support the idea that vision is required to maintain the proper distribution of cells in the L2/3 cell-type continuum and that vision preferentially

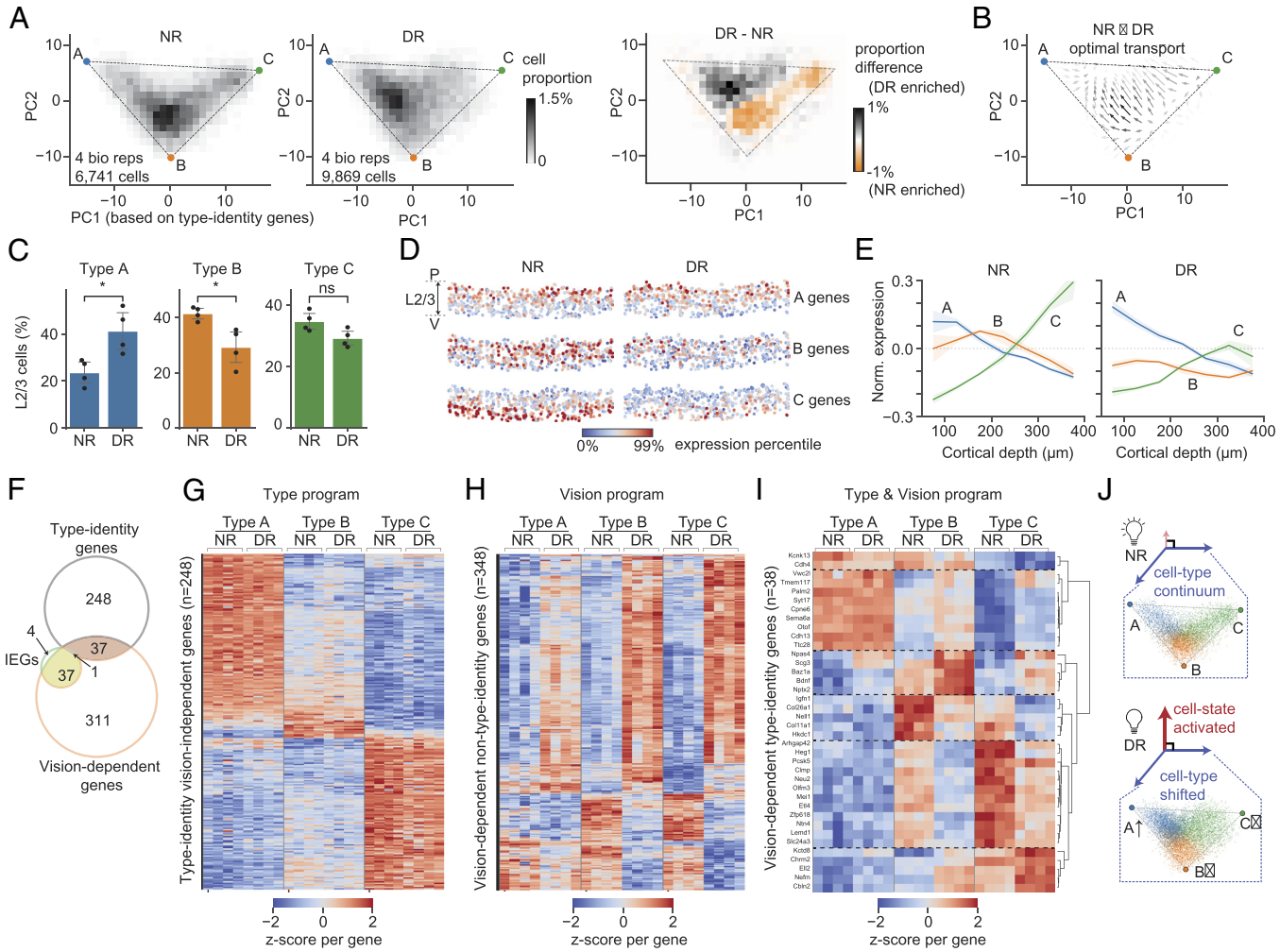

Fig. 4. Visual deprivation redistributes cells within the L2/3 type triangle. (*A*) Distribution of L2/3 types within the L2/3 type-triangle. Cell density for NR cells (*Left*), DR cells (*Middle*), and the difference between NR and DR (*Right*) are shown in PC1 and PC2 space derived from type-identity genes. (*B*) Optimal transport analysis (34, 35) showing the transport map connecting the NR to DR distribution. The arrows indicate the direction of local redistribution of cells in the reduced gene expression space. (*C*) The proportions of L2/3 cells assigned as types A, B, and C for NR and DR samples. The type assignment is based on type A, B, and C identity gene expression (*Materials and Methods*). (*D*) In situ expression levels of A, B, and C type-identity genes for NR and DR samples. (*E*) Expression of A, B, and C identity genes along the P-V axis from upper to lower L2/3 for NR (*Left*) and DR (*Right*) samples. Mean expression levels were shown relative to the baseline levels, which are defined as the mean expression levels in NR samples averaged across L2/3. (*F*) Overlap between vision-dependent genes, type-identity genes, and previously identified L2/3 IEGs (16). (*G–I*) Expression profiles of type-identity vision-*in*dependent genes (*G*), vision-dependent *non*-type-identity genes (*H*), and vision-dependent type-identity genes (*I*). Expression levels are *z*-score normalized across all samples independently for each gene (row). Gene numbers correspond to panel (*F*). (*J*) Diagram shows L2/3 transcriptomes comprise two orthogonal axes of variations–cell-state programs and cell-type programs. Visual deprivation activates cell-state programs and shifts cell-type programs away from archetypes B and C toward A.

impacts types B and C more than type A. The unequal dependence on vision could be related to the spatial zonation, as previous studies have shown that deep, but not more superficial, L2/3 cells receive LGN inputs (37). Consistent with this, our GO analyses suggest that types B and C but not type A genes are enriched in biological processes associated with sensory input (Dataset S3). It remains to be determined whether the vision-dependent programs observed here are specific to developmental plasticity during the critical period or broadly applicable to adult plasticity as well.

Previous studies have shown that neural activity influences the transcriptomes of developing neurons (9, 15, 16, 38–42). Among cortical cell types, L2/3 glutamatergic neurons have been identified as the most sensitive to sensory experience (15, 39), consistent with findings from functional studies (43, 44). Several studies have highlighted the regulation of IEGs under sensory deprivation, although the direction of regulation may depend upon the experimental protocol (9, 16, 39, 40, 42). Our data, based on both snRNA-seq and MERFISH, indicates that dark-rearing leads to an upregulation of IEGs, an effect that is specific to visual areas. Additionally, known IEGs only represent about 10% of genes altered by dark-rearing (Fig. 4*F*). The area-specific nature of the upregulation makes it unlikely to be an experimental artifact, yet the discrepancy in the direction of change compared to some previous studies (39) remains perplexing and warrants systematic investigation in future research.

How the interplay between intrinsic and vision-dependent molecular programs establish the transcriptomic continuum of L2/3 glutamatergic neurons, and how this sculpts circuitry and visual perception are exciting and challenging questions. Emerging techniques correlating transcriptomics, neural activity, and/or connectivity at the single neuron level provide tools to explore these mechanisms (45–48). We anticipate that these studies, alongside modeling and computational analysis, will provide insights into the significance of the continuous nature of cell type variation for the proper function of V1. Multitasking theory (12, 24, 25, 49) suggests that transcriptomic continua aid the division of labor among cells in a tissue responsible for multiple functions. For continua bound by a polygon, cells close to each vertex

(archetype) are specialized for a particular function, while cells in the middle are "generalists," which can perform multiple functions at the cost of being suboptimal for any single function. When gradients in gene expression space are also correlated with position, this can create spatial domains within a tissue, each suited for a unique complement of functions. Consistent with this idea, transcriptomic continua have recently been found to be a common trait in the mammalian brain, and they are often correlated with spatial and physiological continua (21, 50–56). Indeed, the physiological and morphological features of L2/3 neurons in binocular V1 vary as a continuum along the pial–ventricular axis (57). Together, these findings suggest that vision controls the function of L2/3 glutamatergic neurons in V1, at least in part, by contributing to shaping the properties of this continuum. As L2/3 neuron types have selectively expanded in the primate cortex, continua of cell types may be particularly well suited to change by experience and may contribute to the enhanced cognitive capacities of primates.

Materials and Methods

Mice for MERFISH. Mouse breeding and husbandry procedures were carried out in accordance with the animal care and use committee protocol number 2009-031-31A at the University of California, Los Angeles. Mice were given food and water ad libitum and lived in a 12-h day/night cycle with up to four adult animals per cage. Only virgin male C57BL/6 J wild-type mice were used for MERFISH experiments to match with ref. 9.

Visual Deprivation Paradigm. Mice were dark-reared starting P21, which marks the beginning of the ocular dominance critical period. Prior to P21, mice were reared in cages in a room with a 12-h light/dark cycle. At P21, mouse cages were moved to a separate room and placed inside a dark box lined on the inside and the outside with black rubberized fabric (ThorLabs Cat# BK5) with edges sealed by tape and fabric to avoid any light entry. Mice were dark-reared in this setup for 7 d (P21-28DR group). During this period, any handling of the cages was performed in the dark with room lights off, door crevices sealed from exterior light, and in dim red light, which is invisible to the mice. A light meter was used to measure the amount of light inside the dark-rearing box before visual deprivation paradigm. All mice were dark-reared in 0 to 0.01 lx conditions. At the end of dark-rearing, mice were killed and harvested for MERFISH experiments under red light.

Normally reared mice were housed in a 12 h light-ON, 12 h light-OFF cycle and were harvested during a range of 6 to 8 h into the light-OFF phase. The cages of normally reared mice were wrapped with the same black rubberized fabric and carried to dark room with only red light on to minimize light exposure before they were killed.

Tissue Preparation and MERFISH Experiments. All mice were anesthetized with isoflurane and then perfused transcardially with 10 mL heparinized PBS. Following perfusion, the brains were harvested, imbedded in prechilled Tissue-Tek® OCT mounting medium, and flash-frozen in dry ice-prechilled methylbutane. The frozen blocks were then kept on dry ice and stored at −80 °C until time of sectioning. To prepare cryosections for MERFISH, two entire OCT blocks (two brains) or three bisected OCT blocks (three hemibrains) were combined and sectioned at −20 °C in a Leica CM1850 cryostat. Two 12-mm-thick coronal slices (one anterior and one posterior containing binocular V1 with ~550 μm apart in the anterior–posterior axis) were directly collected onto specially coated 4 cm-diameter MERFISH glass slides (merslides, Vizgen Item# 10500001). For locating the visual cortex, atlas coordinates from (Franklin and Paxinos, (58)) and Allen Brain Atlas were used. Collected cryosections on the MERFISH slides (merslides) were fixed in 4% paraformaldehyde in PBS (15 min at RT) in a 6 cm petri dish, rinsed with cold RNase-free PBS, and stored in 70% ethanol at 4 °C until the step of MERFISH probe hybridization.

MERFISH was performed according to Vizgen's instructions. Briefly, merslides with brain sections stored in 70% ethanol were rinsed with Vizgen Sample Preparation Buffer (SPB) after aspiration of 70% ethanol, incubated with Vizgen's Formamide Wash Buffer (FWB, 30 min at 37 °C) followed by MERFISH probe labeling with a customized mouse gene panel containing 500 mouse genes (VZGCP0991, Dataset S2, ~40 h at 37 °C) in a moist chamber, and washed with FWB twice (30 min at 47 °C). The brain sections were be embedded with Vizgen gel mix after removal of FWB, cleared in 5 mL clearing mix solution with 50 mL protease K (overnight at 37 °C), stained with Vizgen DAPI/poly(T) reagent included in the Vizgen 500-gene imaging kit (10 min at RT) after rinse with SPB and FWB (10 min at RT). Then the merslide was thoroughly rinsed with SPB, carefully assembled into an imaging gasket chamber, and uploaded into the MERSCOPE for imaging. The MERFISH imaging was done on the MERSCOPE with an activated Vizgen 500-gene imaging kit after adding the imaging buffer activator and RNase inhibitor (100 mL) as instructed. The imaging process was conducted under the direction of Vizgen's MERSCOPE program (Software version 233.230615.567) with the default settings (both polyT and DAPI channels "on," scan thickness: 10 mm). Once the MERFISH imaging process was completed, the output files were transferred for in-depth analysis with MERFISH Visualizer and in-house custom bioinformatic pipeline.

snRNA-seq Data Processing and Normalization. Cell-by-gene count matrices from the previous study were downloaded from Gene Expression Omnibus (GEO) repository GSE190940 (9). Cell type labels were downloaded from the associated Github repository https://github.com/shekharlab/mouseVC. Raw count matrices were normalized as described before. Transcript counts within each cell were rescaled to sum up to 10,000. A pseudocount of 1 was added to the normalized transcript counts for each gene within each cell, followed by log10-transformation. For PCA and clustering, log10-transformed counts were z-scored across cells for each gene.

We reproduced a list of L2/3 type-identity genes (n = 286, Dataset S1) by following the differential expression analysis used in the previous study. Briefly, the expression of each gene was compared in one type versus others (L2/3 A vs, B to C; L2/3 B vs. A to C; and L2/3 C vs. A to B). We used *scanpy.tl.rank_genes_groups* to identify differentially expressed genes (DEGs) if a gene meets the following criteria: a) false discovery rate (FDR) < 0.05 based on Wilcoxon rank-sum test; b) fold change > 2, and c) the gene was expressed in >30% cells in the up-regulated type.

MERFISH Data Processing and Normalization. Starting from a cell-by-gene matrix, in which each entry is an integer representing the number of transcripts detected in each cell and for a specific gene by MERFISH, we first removed low quality cells. We kept cells with a volume between 50 ~ 2,000, total number of detected transcripts >10, and false positive rate of transcript detection < 5% for the initial analysis. (Later to identify L2/3 cell types A, B, and C, we further selected high-quality cells with total number of detected transcripts > 50). Notably, the false positive rate is a unique feature of MERFISH. In MERFISH experiments, transcripts were identified by binary barcodes extracted from repeated rounds of hybridization, imaging, and puncta detection. A few barcodes were designed to be blank barcodes unmapped to any genes, which allowed us to estimate false positive transcript detection rate. Out of the eight MERFISH sections, four were done on the full coronal sections while the rest were done on hemibrain coronal sections only. For consistency, we computationally cut out a hemi-brain section for every sample for downstream analysis.

Following the same procedure employed in a previous MERFISH study (21), we normalized the raw count matrix first by cell volume and then by mean transcript count across samples such that each section had the same mean number of transcripts (n = 250) detected per cell. This procedure effectively ameliorated cell volume-associated variation and batch effects across samples. After the above cell-to-cell and sample-to-sample size normalization, we normalized the data by log (+1) transformation and z-scored every gene.

Notably, we found a massive upregulation of a panel of IEGs in sections from DR mice compared to NR (see main text). To remove this confounding factor, sample-to-sample normalization was done using 484 out of the 500 genes profiled by MERFISH (excluding the 16 IEGs) to compute the total transcript counts. We found that the identification of major cell subclasses was unaffected by the inclusion/exclusion of IEGs. However, IEG removal helped quantify gene expression changes in NR vs DR within L2/3 types more accurately.

Spatial Domain Analysis. To identify the major anatomical areas and molecular organization within our MERFISH sections, we performed a clustering analysis on each section based on cell-to-cell gene expression similarity and spatial proximity. Using the normalized data as features, we performed a PCA and generated a

gene-expression-similarity graph based on coordinates in the space of the top 50 PCs. We also generated a spatial-proximity graph based on spatial locations of the cells. Both graphs were generated using *scanpy.pp.neighbors* following default parameters. We generated a spatial-and-gene hybrid graph by blending the spatial and the gene graphs with equal weighting. We applied Leiden clustering on the hybrid graph using *scanpy.tl.leiden* following default parameters. The resulting spatial domains recover major anatomical structures in the mouse brain, which were visualized in Fig. 1 and *SI Appendix*, Fig. S1. Clusters were annotated based on anatomical and molecular features.

Establishing Curved Cortical Coordinates and Identifying V1. We developed an automated iterative procedure to fit a smooth curve along the pial surface, which served as a reference line to establish curved coordinate system along the vertical (pia-ventricular; P-V) and the tangential (medial–lateral; M-L) axis of the cortex.

We took advantage of meningeal cells (VLMCs), which specifically express *Slc6a13* and are located along the pial surface. Using these *Slc6a13*+ cells as anchors, we first fit a fourth-order polynomial using *numpy.polyfit*. Subsequently, we used the fitted line as a reference to calculate the depth for all the anchor cells. Anchor cells whose depth that are >1/2 of the maximum depth (robust maximum taken as the 95% max depth) among all anchors were removed from the set of anchor cells for another round of more refined fitting. This procedure was repeated for 5 ~ 10 times until the inferred reference line was stable and visually matched the cortical surface. Using the reference line, all cortical cells were assigned a depth along the P-V axis and a width along the M-L axis.

Using the curved coordinates, cortical cells, defined as having cortical depth less than 1,100 microns from the pial surface, were extracted from the full coronal sections for downstream analysis. V1 cells were identified based on tangential locations based on areal-specific markers mentioned in the main text.

Identification of Subclasses of V1 Cells and Integration with Published snRNA-seq Data. To systematically identify major cell populations, V1 cells were extracted and merged from all MERFISH sections (eight in total for this study; NR and DR) as mentioned above and were integrated with our previously published snRNA-seq data (9) using Harmony (18). We did this at two levels—the class level and the subclass level within the excitatory and inhibitory classes (*SI Appendix*, Fig. S1).

To integrate the MERFISH and snRNA-seq data (P28NR), we intersected MERFISH genes (n = 484, excluding IEGs) and highly variable genes (HVGs; n = 7,340) identified by snRNA-seq, which resulted in 361 overlapping genes between the two datasets. For this analysis, we only used high-quality MERFISH cells, defined as cells with at least 50 transcripts. We computed PCA (n = 20 components) using cells from both datasets based on the overlapping genes (z-scored separately for each dataset). We then applied Harmony using *scanpy.external.pp.harmony_integrate* to generate harmonized PCs.

These harmonized PCs were used for downstream visualization and cell-type assignment. UMAP were generated using *scanpy.pl.umap* with the default parameters. Cell type labels were transferred from the published snRNA-seq data to MERFISH based on k-nearest-neighbor-based assignment using *sklearn.neighbors.NearestNeighbors*. A MERFISH cell was assigned to the most frequent cell class out of its k = 100 snRNA-seq neighbors. To assign cell subclasses with a cell class, k = 30 neighbors were used.

A small fraction of MEFISH cells could not be confidently assigned a cell class (*SI Appendix*, Fig. S1*C*). These cells were defined as those whose k = 100 neighbors in the harmonized PCs contains ≤ 2 cells from snRNA-seq, indicating an unsuccessful data integration for these cells. These cells were assigned label "NA" (*SI Appendix*, Fig. S1), most likely being low-quality nonneuronal cells with lower number of transcripts, and unspecific spatial signatures. They were mostly grouped with microglia and endothelial cells in the UMAP embedding (*SI Appendix*, Fig. S1*C*).

Identification of L2/3 Glutamatergic Cell Types. The procedures above identified all cell subclasses, among which we focused on one subclass, the L2/3 glutamatergic neurons, for further analysis. Two strategies were used to further identify the three types of L2/3 neurons (types A, B, and C). The first was to repeat the analysis above at the cell type level, which assigned each MERFISH cell an identity based on its k-nearest neighboring snRNA-seq cells in the harmonized PC space.

We also used a second strategy, which offers more biological interpretability. Given the continuous nature of L2/3 types bounded by the three archetypes A, B, and C, we developed continuous A-B-C scores based on the expression levels of type-A, B, and C identity genes (n = 170 profiled by MERFISH). Each cell was assigned three scores (p_a, p_b, p_c), with $p_a + p_b + p_c = 1$, representing the probabilities that this cell belongs to type A, B, and C, respectively. For a cell i, we first characterized its overall expression levels of type-A specific genes by the mean z-scored type-A-identity gene expression,

$$z_{ia} = \frac{1}{|G_a|} \sum_{g \in G_a} z_{ig},$$

where G_a represents the set of type-A-identity genes and $|G_a|$ represents its size. Type B and C scores were similarly defined as

$$z_{ib} = \frac{1}{|G_b|} \sum_{g \in G_b} z_{ig},$$

$$z_{ic} = \frac{1}{|G_c|} \sum_{g \in G_c} z_{ig},$$

These mean z-scores were normalized to be bounded between [0, 1].

$$s_{ia} = \frac{|z_{ia} - z_{\min,a}|}{z_{max,a} - z_{min,a}},$$

where $z_{min,a}$ is defined as the 40th percentile of z_{ia} among L2/3 cells and $z_{max,a}$ is defined as the 95th percentile. Next, we normalized these scores such that they sum to 1,

$$p_{ia} = \frac{s_{ia}}{s_{ia} + s_{ib} + s_{ic}},$$

These scores can be directly visualized at single-cell level using an additive blending between three (archetypal) colors. To assign discrete cell type labels, one can also assign a cell to the type that has the highest ABC scores. Cells with clear A, B, or C identity, i.e. archetypal cells, are defined as those whose highest ABC scores were greater than 0.6 ($\max(p_a, p_b, p_c) > 0.6$).

Pseudotime Analysis for the L2/3 Transcriptomic Continuum. We computed pseudotemporal coordinates for L2/3 cells to understand their continuous organization. We first computed the top 50 PCs using z-scored L2/3 type-identity genes, and generated a k-nearest-neighbor (k = 50) graph between cells in the PC space. The graph was built using the function *Scanpy.pp.neighbors*. Next, we ran a diffusion map (22) using *Scanpy.tl.diffmap* and ran diffusion pseudotime using *scanpy.dpt* following default parameters. The cell with the smallest PC1 was assigned as the root cell and serves as the starting point of diffusion. As a result, each cell was assigned a pseudotemporal coordinate, and cells were ranked by the increasing order of pseudotime.

We also ranked L2/3 type-identity genes according to their expression along the pseudotime coordinates. We defined the pseudotime of a gene (T_g) as the weighted average of cell pseudotime,

$$T_g = \sum_c w_{gc} t_c,$$

where t_c is the pseudotime of the cell (c), and w_{gc} is the weight of the cell c contributing to the gene g. The weight of a gene is defined by its expression level and sums to 1,

$$w_{gc} = \frac{x_{gc}}{\sum_{c'} x_{gc'}},$$

where x_{gc} is the size and log normalized expression. This gene pseudotime was defined at P28NR and was kept fixed to give a consistent representation for comparisons between conditions.

Archetypal Analysis (the Multitasking Framework). We used the python package *py_pcha*: https://github.com/ulfaslak/py_pcha to determine the geometry of the L2/3 cell type continuum in the PC1-PC2 space derived from the L2/3

type-identity genes. The tool uses archetypal analysis, also known as the principal convex hull analysis, to infer a triangular boundary to the L2/3 transcriptomes. The same procedure (with parameters *delta* = 0 and *noc* = 3) was applied to different combinations of data (snRNA-seq, MERFISH, different conditions, harmonized data, and shuffled data; see main text).

We evaluated the significance of the triangular fit by the t-ratio test as proposed by the multitasking framework (12). T-ratio is the ratio between the area of the convex hull of the data and that of the principal convex hull (the triangular bound in our case). We calculated the area of the convex hull using the python package *scipy* and its function *scipy.spatial.ConvexHull*. We tested the significance of the observed t-ratio by comparing it to t-ratios of shuffled data by permuting each gene independently across all cells. *P*-value was computed based on 1,000 shuffles.

Simulations of Continuous and Discrete Types. First, we describe our procedure to simulate transcriptomic continua. Let cells and genes be ranked, such cells with a particular ranking express genes with a similar ranking. Let i be an integer representing the cell ranking, which ranges from 1 to N_c, with N_c denoting the total number of cells. Let j be an integer representing the gene ranking, which ranges from 1 to N_g, with N_g denoting the total number of genes. We use $p_i = {}^{i}/_{N_c}$ and $p_j = {}^{j}/_{N_g}$ to represent the normalized rankings such that both the gene rankings and cell rankings range from 0 to 1. We consider a model where the expected expression level of gene j in cell i is a Gaussian such that

$$\lambda_{ij} = e^{-\left(\frac{p_i - p_j}{\varepsilon}\right)^2},$$

where ε denotes the level of noise. Gene counts are then drawn from a scaled Poisson distribution parameterized by λ_{ij}:

$$c_{ij} \sim s \cdot Poisson\left(\lambda_{ij}\right).$$

For our simulation, we chose $N_g = 60, N_c = 600, s = 100$, with different ε values between 0.1 and 1. Random numbers were generated using the python package *numpy.random*.

Second, for simulating discrete types, we assumed a model wherein each type is distinguished by a set of "marker" genes. Let i be a cell and $C(i)$ be the cell type it belongs to. Let j be a gene and $C\left(j\right)$ be the cell type of which it is a marker. The expected expression level of gene j in cell i was modeled by a binary matrix:

$$\lambda_{ij} = \begin{cases} 1 if C(i) = C\left(j\right) \\ \varepsilon if C(i) \neq C\left(j\right) \end{cases},$$

where ε denotes the amount of leaky expression, i.e., the level of noise. ε takes values between 0 and 1. The larger ε is, the noisier the types are. The actual count matrix was drawn from a scaled Poisson distribution parameterized by λ_{ij},

$$c_{ij} \sim s \cdot Poisson\left(\lambda_{ij}\right).$$

We simulated three discrete types (A, B, C), each with 20 marker genes and containing 200 cells, with different ε values between 0.1 and 1. To assign an order between types, among the 20 marker genes, 6 were shared between neighboring types, such that 6 type-A markers were also expressed in type B, and 6 type-B markers were also expressed in type C, and so on.

Aligning V1 Coordinates across Sections. In our samples, V1 spanned about 2 mm (or ~2,000 microns) along the tangential (M-L) axis of the cortex, with different sections having different lengths as defined by the expression domains of V1 marker genes *Scnn1a* and *Igfbp4* (see Main text). To quantify the in situ patterns of specific genes within V1 and in other cortical regions across samples, we defined a normalized tangential coordinate system relative to the length of V1. Specifically, for each section we used the tangential locations of the two ends of V1, t_m and t_l, to normalize tangential coordinates along the cortex:

$$\tilde{t} = \frac{t - t_m}{t_l - t_m},$$

In this normalization, 0 and 1 represent the two ends of V1 (medial-most and lateral-most) respectively. And values <0 and 0 > 1 represent regions outside of (flanking) V1. Expression levels of specific genes are quantified according to this normalized coordinate system.

Focused Clustering. In addition to the cell types identified previously, we applied K-means clustering (*sklearn.cluster.Kmeans*) using only L2/3 type-identity genes as features, to identify focused clusters. As mentioned in the main text, the motivation of this analysis is to uncover L2/3 cell types in DR while ignoring changes to other gene programs related to cell states. This procedure generates matched cell types between NR and DR.

PCA. We applied PCA using *sklearn.decomposition.PCA*. In Fig. 3, we applied it on L2/3 glutamatergic neurons combined from both P28NR and P28DR mice, using a set of unbiasedly identified highly variable genes (HVGs) as features. For HVGs identification, we considered n = 21,222 genes that had nonzero counts in at least 10 cells. For each gene, we computed the variance-mean ratio on counts-per-10 k-transcripts (CP10k) normalized data. Under a Poisson distribution, this variance-mean ratio is expected to be a constant. Indeed, this value is stable across orders of magnitude difference in mean expression across genes. To select HVGs with different baseline (mean) expressions, we grouped genes into decile-bins according to mean expression, and for each bin, we selected the top 30% genes with the most variance-mean ratio. N = 6,360 genes were selected, and most (n = 270/286) L2/3 type-specific genes are part of the HVGs.

In Fig. 4, we applied PCA using L2/3 type-identity genes (n = 286; Dataset S1) as features. Focusing on L2/3 type-identity genes, rather than HVGs, allowed us to study the impact of visual deprivation on the L2/3 type-identity gene programs, while ignoring changes to other gene programs.

We evaluated the degree of overlap between two PCA eigenvectors v_i and v_j as the absolute value of their dot product ($\left|v_i \cdot v_j\right|$). As the eigenvectors are orthonormal, this value is bounded between 0 and 1.

GO Analysis. We used the tool *EnrichR*: https://maayanlab.cloud/Enrichr/ for GO analysis. All enrichment analyses were performed by comparing a gene list of interest with a background set of top 5,000 most expressed genes in L2/3 (P28NR). Top 10 enriched GO terms of Biological Process (2023 version) that were statistically significant with FDR < 0.05 were shown. For terms belonging to the same branch (parents or children), only one term with the highest FDR was shown in the main figures to reduce redundancy. Terms annotated as "obsolete" according to quickGO (https://www.ebi.ac.uk/QuickGO/annotations) were also removed from the main figures. All enriched terms (unfiltered) are shown in supplementary figures.

Previously Identified L2/3 Stimulus–Response Genes. Hrvatin et al. (16) reported 611 stimulus–response genes identified from different cell types in V1, among which we filtered out those that are related to L2/3 glutamatergic neurons (labeled as "ExcL23" in ref. 16), including 42 early-response genes and 37 late-response genes. These genes are listed in Dataset S5.

We used the Fisher exact test with n = 6,360 HVGs as the background to test for enrichment or depletion of the overlap between PC-driving genes and the above activity-regulated genes.

Quantification of Cell Redistribution in DR. We profiled the cell-density distributions of L2/3 cells in PC1 to PC2 space derived from type-identity genes using the python package *seaborn.histplot*. The distributions were robust across a range of bin widths, and we used bin-widths of 1 ~ 1.5 for visualization. We used the Jensen–Shannon (JS) divergence (59) to measure the level of difference in cell-density distributions between NR and D and across samples. This metric was calculated using *scipy.spatial.distance.jensenshannon*.

Optimal transport analysis was performed using the python package *POT*: https://pythonot.github.io/. The program computes the optimal transport map (35, 60) connecting the empirical distributions of NR cells and DR cells in PC1 to PC2 space derived from type-identity genes. We first used *ot.dist* to compute pairwise distance matrix between NR and DR cells with default parameters. We then used *ot.emd* to calculate the transport map. The result was a matrix whose elements denote transport couplings between each pair of NR and DR cells, a proxy for their transcriptomic correspondence. We visualized this result by a coarse-grained vector field as follows. First, the PC1 to PC2 space was meshed into equal-sized 2D bins. For each 2D bin, we computed a vector representing the mean moving direction and magnitude for all cells that fall into the bin. The vectors are visualized by arrows whose direction represents the average moving directions among local cells, whose lengths are proportional to the movement magnitudes, and whose color (darkness) is proportional to the number of cells represented by the bins.

Identification of DEGs between NR and DR. In scRNA-seq analysis, it is common to treat individual cells as samples in statistical tests for identifying DEGs. This approach often leads to many statistically significant genes as even modest effect sizes can appear unlikely (low *P*-values) under the "no effect" null hypothesis owing to large cell numbers. Therefore, as a conservative measure to identify DEGs between NR and DR, we chose to regard the biological samples, rather than single cells, as independent data points.

We compared NR vs. DR across independent biological samples, with each condition having four independent biological samples: P28 rep1, P28 rep2, P38 rep1, and P38 rep2. Raw counts from cells of the same types and samples were aggregated to produce pseudobulk profiles. We only considered genes with mean expression (in counts per million transcripts; CPM) > 10 in at least one type in either NR or DR. We performed an independent-sample t-test (*scipy.stats.ttest_ind*) on the pseudobulk profiles between NR and DR for each type. The resulting *P*-values were adjusted by the Benjamini–Hochberg procedure to calculate the FDR. Effect sizes were quantified as the log2 fold change (in CPM) in DR compared with NR. DEGs were defined as those with $FDR < 0.05$ and $|\log_2 FC| > 1$.

Data, Materials, and Software Availability. MERFISH data generated by this study was deposited on Zenodo with DOI: 10.5281/zenodo.13916878 (14). snRNA-seq data was downloaded from GEO with the accession number GSE190940 (10). Code to reproduce L2/3 type specific genes (Dataset S1, n = 286) was obtained from the GitHub repository: https://github.com/shekharlab/mouseVC (11). Code to reproduce the figures in the manuscript was deposited in the following GitHub repository: https://github.com/FangmingXie/vision_and_visctx (61). A standalone software including a step-by-step tutorial to reproduce the Archetypal Analysis and its associated statistical tests described in the manuscript was deposited in the following GitHub repository: https://github.com/FangmingXie/SingleCellArchetype (26). All other data are included in the manuscript and/or supporting information.

ACKNOWLEDGMENTS. We thank members of the Zipursky lab for critical feedback. This work was supported by a grant from the W.M. Keck Foundation to S.L.Z., a NIH grant 1F31 NS131016 to S.B., the Hellman Foundation (K.S.), and McKnight Foundation (K.S.). K.S. is an investigator with the Glaucoma Research Foundation and is supported by the Melza M. and Frank Theodore Barr Foundation. S.L.Z. is an investigator of the Howard Hughes Medical Institute.

Author affiliations: [a]Department of Biological Chemistry, David Geffen School of Medicine, University of California, Los Angeles, CA 90095; [b]School of Biological Sciences, Georgia Institute of Technology, Atlanta, GA 30332; [c]Department of Chemical and Biomolecular Engineering, University of California, Berkeley, CA 94720; [d]Helen Wills Neuroscience Institute, University of California, Berkeley, CA 94720; [e]Department of Anatomy and Neurobiology, Center for Neural Circuit Mapping, Institute for Memory Impairments and Neurological Disorders, University of California, Irvine, CA 92697; and [f]Biological Systems and Engineering Division, Lawrence Berkeley National Laboratory, Berkeley, CA 94720

1. T. N. Wiesel, D. H. Hubel, Single-cell responses in striate cortex of kittens deprived of vision in one eye. *J. Neurophysiol.* **26**, 1003–1017 (1963).
2. T. K. Hensch, Critical period regulation. *Annu. Rev. Neurosci.* **27**, 549–579 (2004).
3. L. E. White, D. Fitzpatrick, Vision and cortical map development. *Neuron* **56**, 327–338 (2007).
4. J. S. Espinosa, M. P. Stryker, Development and plasticity of the primary visual cortex. *Neuron* **75**, 230–249 (2012).
5. B. M. Hooks, C. Chen, Circuitry underlying experience-dependent plasticity in the mouse visual system. *Neuron* **106**, 21–36 (2020).
6. J. A. Gordon, M. P. Stryker, Experience-dependent plasticity of binocular responses in the primary visual cortex of the mouse. *J. Neurosci.* **16**, 3274–3286 (1996).
7. L. Tan, E. Tring, D. L. Ringach, S. L. Zipursky, J. T. Trachtenberg, Vision changes the cellular composition of binocular circuitry during the critical period. *Neuron* **108**, 735–747.e6 (2020).
8. B.-S. Wang, R. Sarnaik, J. Cang, Critical period plasticity matches binocular orientation preference in the visual cortex. *Neuron* **65**, 246–256 (2010).
9. S. Cheng *et al.*, Vision-dependent specification of cell types and function in the developing cortex. *Cell* **185**, 311–327.e24 (2022).
10. S. Cheng *et al.*, Vision-dependent specification of cell types and function in the developing cortex. NCBI-GEO. https://www.ncbi.nlm.nih.gov/geo/query/acc.cgi?acc=GSE190940. Deposited 27 December 2021.
11. S. Cheng *et al.*, Vision-dependent specification of *cell* types and function in the developing cortex. GitHub. https://github.com/shekharlab/mouseVC. Accessed 10 October 2024.
12. M. Adler, Y. Korem Kohanim, A. Tendler, A. Mayo, U. Alon, Continuum of gene-expression profiles provides spatial division of labor within a differentiated cell type. *Cell Syst.* **8**, 43–52.e5 (2019).
13. K. H. Chen, A. N. Boettiger, J. R. Moffitt, S. Wang, X. Zhuang, RNA imaging. Spatially resolved, highly multiplexed RNA profiling in single cells. *Science* **348**, aaa6090 (2015).
14. F. Xie *et al.*, MERFISH data of the developing mouse visual cortex under normal- and dark-rearing. Zenodo. https://doi.org/10.5281/zenodo.13916877. Deposited 10 October 2024.
15. X. Chen *et al.*, Whole-cortex in situ sequencing reveals input-dependent area identity. *Nature*, 1–10 (2024), 10.1038/s41586-024-07221-6.
16. S. Hrvatin *et al.*, Single-cell analysis of experience-dependent transcriptomic states in the mouse visual cortex. *Nat. Neurosci.* **21**, 120–129 (2017), 10.1038/s41593-017-0029-5.
17. S.-J. Chou *et al.*, Geniculocortical input drives genetic distinctions between primary and higher-order visual areas. *Science* **340**, 1239–1242 (2013).
18. I. Korsunsky *et al.*, Fast, sensitive and accurate integration of single-cell data with Harmony. *Nat. Methods* **16**, 1289–1296 (2019), 10.1038/s41592-019-0619-0.
19. S. Sahara, Y. Yanagawa, D. D. M. O'Leary, C. F. Stevens, The fraction of cortical GABAergic neurons is constant from near the start of cortical neurogenesis to adulthood. *J. Neurosci.* **32**, 4755–4761 (2012).
20. Z. Yao *et al.*, A high-resolution transcriptomic and spatial atlas of cell types in the whole mouse brain. *Nature* **624**, 317–332 (2023).
21. M. Zhang *et al.*, Molecularly defined and spatially resolved cell atlas of the whole mouse brain. *Nature* **624**, 343–354 (2023).
22. L. Haghverdi, M. Büttner, F. A. Wolf, F. Buettner, F. J. Theis, Diffusion pseudotime robustly reconstructs lineage branching. *Nat. Methods* **13**, 845–848 (2016).
23. R. R. Coifman *et al.*, Geometric diffusions as a tool for harmonic analysis and structure definition of data: Diffusion maps. *Proc. Natl. Acad. Sci. U.S.A.* **102**, 7426–7431 (2005).
24. U. Alon, *An Introduction to Systems Biology: Design Principles of Biological Circuits* (Chapman & Hall/CRC, ed. 2, 2019).
25. M. Adler *et al.*, Emergence of division of labor in tissues through cell interactions and spatial cues. *Cell Rep.* **42**, 112412 (2023).
26. F. Xie *et al.*, Archetypal analysis of single-cell RNA-seq data. GitHub. https://github.com/FangmingXie/SingleCellArchetype. Accessed 29 January 2024.
27. N. Eling, M. D. Morgan, J. C. Marioni, Challenges in measuring and understanding biological noise. *Nat. Rev. Genet.* **20**, 536–548 (2019), 10.1038/s41576-019-0130-6.
28. O. Hobert, Terminal selectors of neuronal identity. *Curr. Top. Dev. Biol.* **116**, 455–475 (2016).
29. E. J. Kim *et al.*, Extraction of distinct neuronal cell types from within a genetically continuous population. *Neuron* **107**, 274–282.e6 (2020).
30. B. J. Molyneaux *et al.*, DeCoN: Genome-wide analysis of in vivo transcriptional dynamics during pyramidal neuron fate selection in neocortex. *Neuron* **85**, 275–288 (2015).
31. Y.-H. Chuang *et al.*, Parkinson's disease is associated with DNA methylation levels in human blood and saliva. *Genome Med.* **9**, 76 (2017).
32. Y. Z. Kurmangaliyev, J. Yoo, J. Valdes-Aleman, P. Sanfilippo, S. L. Zipursky, Transcriptional programs of circuit assembly in the Drosophila visual system. *Neuron* **108**, 1045–1057.e6 (2020).
33. M. N. Özel *et al.*, Neuronal diversity and convergence in a visual system developmental atlas. *Nature* **589**, 88–95 (2021).
34. R. Flamary *et al.*, POT: Python optimal transport. *J. Mach. Learn. Res.* **22**, 1–8 (2021).
35. G. Schiebinger *et al.*, Optimal-transport analysis of single-cell gene expression identifies developmental trajectories in reprogramming. *Cell* **176**, 928–943.e22 (2019).
36. K. D. Harris, G. M. G. Shepherd, The neocortical circuit: Themes and variations. *Nat. Neurosci.* **18**, 170–181 (2015).
37. N. A. Morgenstern, J. Bourg, L. Petreanu, Multilaminar networks of cortical neurons integrate common inputs from sensory thalamus. *Nat. Neurosci.* **19**, 1034–1040 (2016).
38. Q. Lo Giudice, R. J. Wagener, P. Abe, L. Frangeul, D. Jabaudon, Developmental emergence of first- and higher-order thalamic neuron molecular identities. *Development* 151, dev202764 (2024).
39. A. M. Xavier, Q. Lin, C. J. Kang, L. Cheadle, A single-cell transcriptomic atlas of sensory-dependent gene expression in developing mouse visual cortex. bioRxiv [Preprint] (2024). https://doi.org/10.1101/2024.06.25.600673 (Accessed 26 January 2025).
40. S. Butrus, H. R. Monday, C. J. Yoo, D. E. Feldman, K. Shekhar, Molecular states underlying neuronal cell type development and plasticity in the whisker cortex. bioRxiv [Preprint] (2024). https://doi.org/10.1101/2024.10.07.617106 (Accessed 26 January 2025).
41. D. Tropea *et al.*, Gene expression changes and molecular pathways mediating activity-dependent plasticity in visual cortex. *Nat. Neurosci.* **9**, 660–668 (2006).
42. M. Majdan, C. J. Shatz, Effects of visual experience on activity-dependent gene regulation in cortex. *Nat. Neurosci.* **9**, 650–659 (2006).
43. M. E. Diamond, W. Huang, F. F. Ebner, Laminar comparison of somatosensory cortical plasticity. *Science* **265**, 1885–1888 (1994).
44. D. E. Feldman, M. Brecht, Map plasticity in somatosensory cortex. *Science* **310**, 810–815 (2005).
45. S. Xu *et al.*, Behavioral state coding by molecularly defined paraventricular hypothalamic cell type ensembles. *Science* **370**, eabb2494 (2020).
46. C. Condylis *et al.*, Dense functional and molecular readout of a circuit hub in sensory cortex. *Science* **375**, eabl5981 (2022).
47. J. W. Kim *et al.*, Molecular recording of calcium signals via calcium-dependent proximity labeling. *Nat. Chem. Biol.* **20**, 894–905 (2024).
48. Z. Jiao *et al.*, Projectome-defined subtypes and modular intra-hypothalamic subnetworks of peptidergic neurons. bioRxiv [Preprint] (2023). https://doi.org/10.1101/2023.05.25.542241 (Accessed 26 January 2025).
49. O. Shoval *et al.*, Evolutionary trade-offs, Pareto optimality, and the geometry of phenotype space. *Science* **336**, 1157–1160 (2012).
50. M. Zhang *et al.*, Spatially resolved cell atlas of the mouse primary motor cortex by MERFISH. *Nature* **598**, 137–143 (2021).
51. G. Stanley, O. Gokce, R. C. Malenka, T. C. Südhof, S. R. Quake, Continuous and discrete neuron types of the adult murine striatum. *Neuron* **105**, 688–699.e8 (2020).
52. B. Tasic *et al.*, Shared and distinct transcriptomic cell types across neocortical areas. *Nature* **563**, 72–78 (2018).
53. K. D. Harris *et al.*, Classes and continua of hippocampal CA1 inhibitory neurons revealed by single-cell transcriptomics. *PLoS Biol.* **16**, e2006387 (2018).

54. V. Kozareva *et al.*, A transcriptomic atlas of mouse cerebellar cortex comprehensively defines cell types. *Nature* **598**, 214–219 (2021).
55. Y. Li *et al.*, Distinct subnetworks of the thalamic reticular nucleus. *Nature* **583**, 819–824 (2020).
56. M. S. Cembrowski *et al.*, Spatial gene-expression gradients underlie prominent heterogeneity of CA1 pyramidal neurons. *Neuron* **89**, 351–368 (2016).
57. S. Weiler *et al.*, Functional and structural features of L2/3 pyramidal cells continuously covary with pial depth in mouse visual cortex. *Cereb. Cortex* **33**, 3715–3733 (2023).
58. G. Paxinos, K. B. J. Franklin, *Paxinos and Franklin's the Mouse Brain in Stereotaxic Coordinates* (Academic Press, San Diego, CA, 2019).
59. T. M. Cover, J. A. Thomas, *Elements of Information Theory: Cover/Elements of Information Theory* (John Wiley & Sons, ed. 2, 2006).
60. C. Villani, *Optimal Transport: Old and New* (Springer Berlin Heidelberg, 2008).
61. F. Xie *et al.*, Analysis code for the paper "Spatial profiling of the interplay between cell type– and vision–dependent transcriptomic programs in the visual cortex". GitHub. https://github.com/FangmingXie/vision_and_visctx. Accessed 29 January 2024.